Bifurcations from Taylor vortices between corotating concentric cylinders

J. J. Hegseth
Department of Physics, University of New Orleans, New Orleans, Louisiana 70148

G. W. Baxter
Physics Department, Behrend College, Pennsylvania State University at Erie, Erie, Pennsylvania 16563

C. D. Andereck
Department of Physics, Ohio State University, Columbus, Ohio 43210

(Received 10 July 1995)

Taylor vortex flow between corotating concentric cylinders bifurcates to a variety of wavy vortex flows. We have experimentally studied the vicinity of onset of these flows as the axial wavelength, the inner cylinder speed, and the outer cylinder speed are changed. The selection of secondary flows depends strongly on the Taylor vortex size. At small Taylor vortex wavelength an $m=1$ mode as well as a combination of modes are described. The wavy flows are the result of secondary instabilities that develop either at the inflow boundary, the outflow boundary, or inside of vortices near their cores.

PACS number(s): 47.32.−y

I. INTRODUCTION

The Taylor-Couette system consists of two independently rotating concentric cylinders with a fluid-filled gap. The simplicity and symmetry of the geometry and the richness of the observed flow behavior have made it a popular system for studying nonequilibrium transitions leading to spatiotemporal turbulence [1,2]. However, much of the behavior remains poorly understood, particularly when the outer cylinder rotates. In this paper we will systematically explore the effects of varying the inner and outer cylinder rotation rates and the wavelength of the fundamental pattern on the emergence of secondary flows.

Previous studies [2–4] have revealed differing sequences of flow transitions in the corotating and counter-rotating cases. For infinitely long cylinders the base flow in either case is the well-known circular Couette flow with an azimuthal velocity that varies with radius as [5] $V(r)=Ar+B/r$. Neglecting end effects, the primary instability of the base flow, in the corotating case, results in an axially uniform time independent system of axisymmetric Taylor vortices [Taylor vortex flow (TVF)], as shown in Fig. 1. For our purposes, the driving of the flow by the inner cylinder is characterized by the inner cylinder Reynolds number $R_i=\Omega_i r_i d/\nu$, where Ω_i is the inner cylinder angular velocity, r_i is the outer radius of the inner cylinder, r_o is the inner radius of the outer cylinder, $d=r_o-r_i$ is the gap between the cylinders, and ν is the kinematic viscosity. The corresponding parameter for the outer cylinder is the Reynolds number $R_o=\Omega_o r_o d/\nu$, where Ω_o is the outer cylinder angular velocity.

As R_o and R_i are varied Taylor vortices become unstable to various types of azimuthal traveling waves. The specific pattern that appears depends on R_o and R_i. At low R_o, when R_i is increased sufficiently, the wavy vortex

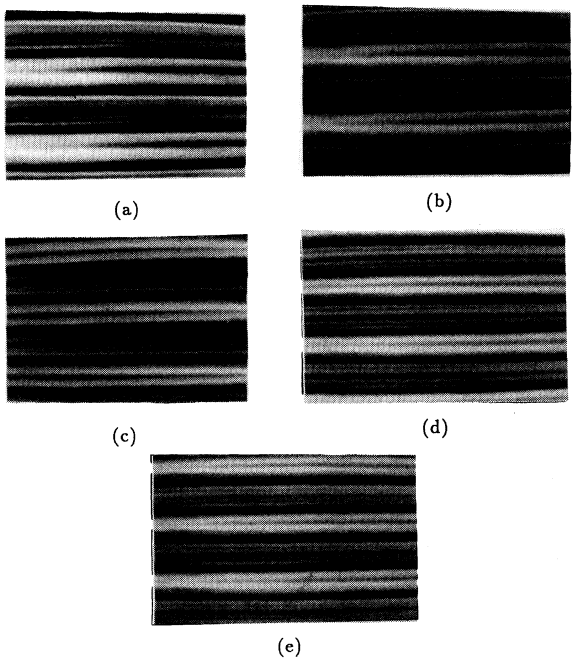

FIG. 1. Shown are the following photographs of Taylor vortex flows (TVF): (a) at $R_0=400$, $R_i=900$, and $\bar{\lambda}=250$; (b) at $R_0=500$, $R_i=1000$, and $\bar{\lambda}=2.31$; (c) at $R_o=500$, $R_i=1100$, and $\bar{\lambda}=2.14$; (d) at $R_o=400$, $R_i=1450$, and $\bar{\lambda}=2.00$; (e) at $R_o=350$, $R_i=1000$, and $\bar{\lambda}=1.88$. The azimuthal direction is along the parallel black lines (horizontal) and the axial direction is perpendicular to these lines (vertical). The black parallel lines are inflow and outflow boundaries. Between these black lines are vortices. Adjacent to each vortex is another vortex that circulates in the opposite sense. Neighboring vortices appear darker or lighter. Below each bright vortex is an outflow boundary and above each bright vortex is an inflow boundary. The distortion along the azimuth is due to the refraction effects in viewing the flow through the cylindrical outer cylinder.

flow (WVF) pattern appears and this pattern, shown in Fig. 2, is characterized by a strong distortion of each vortex. The inflow and outflow boundary waves travel together with the same azimuthal wave number and wave speed but with a constant phase difference between them. At higher R_o, when R_i is increased sufficiently, the TVF pattern bifurcates to one or a combination of the following azimuthal traveling wave patterns: the wavy inflow boundaries (WIB) pattern, the wavy outflow boundaries (WOB) pattern, or the twisted vortices (TWI) pattern (see Figs. 3 and 4) [2,4]. The WIB and WOB are, as their names suggest, azimuthal traveling waves which appear localized near the inflow boundaries or the outflow boundaries of the vortices. WIB and WOB are subharmonic with respect to the axial wavelength, i.e., waves on adjacent inflow (or outflow) boundaries are out of phase, so that the pattern repeats itself every four cells or two wavelengths (one axial wavelength consists of two cells because adjacent cells circulate in opposite senses). The TWI pattern, which gives each vortex the appearance of braided rope, consists of azimuthal traveling waves that are localized inside the vortices, leaving the inflow and outflow boundaries stationary. In addition to these patterns we have observed low amplitude time dependent motion that is also confined to the interior of the vortices. Several of these flows and their interactions have been investigated numerically [6–9] and analytically [10–12]. We restrict ourselves to these secondary, and some tertiary, bifurcations, since the flows beyond these become considerably more complicated to experimentally characterize and are presently less accessible to theory.

It is well known that the wavelength of rolls in Rayleigh-Bénard convection and vortices in the Taylor-Couette system influences the nature and location in parameter space of the secondary bifurcations [2,13]. We have pursued this observation by systematically varying the wavelength of the Taylor vortices above and below the critical wavelength. The critical size cells, which have an approximately square cross section, are obtained when the inner cylinder is slowly ramped from Couette flow to somewhat above the Rayleigh stability line [5]. At the critical wavelength (approximately twice the gap) WVF, WIB, WOB, and TWI are all present as secondary bifurcations (see Fig. 5). For low outer cylinder speeds TVF always bifurcates to WVF although the axial wavelength does affect the particular onset values. Increasing the outer cylinder rotation rate stabilizes TVF against WVF. For large outer cylinder speeds there is a long

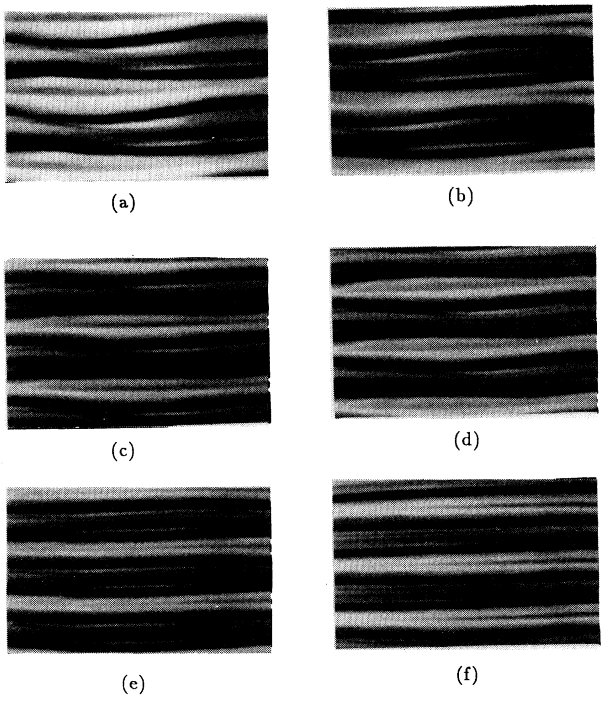

FIG. 2. Shown are the following photographs of wavy vortex flows (WVF): (a) at $R_o=250$, $R_i=900$, and $\bar{\lambda}=2.50$; (b) at $R_0=300$, $R_i=1000$, and $\bar{\lambda}=2.31$; (c) at $R_o=300$, $R_i=1100$, and $\bar{\lambda}=2.14$; (d) at $R_o=300$, $R_i=1450$, and $\bar{\lambda}=2.00$; (e) at $R_o=200$, $R_i=900$, and $\bar{\lambda}=1.88$; (f) $m=1$ at $R_o=350$, $R_i=1100$, and $\bar{\lambda}=1.88$.

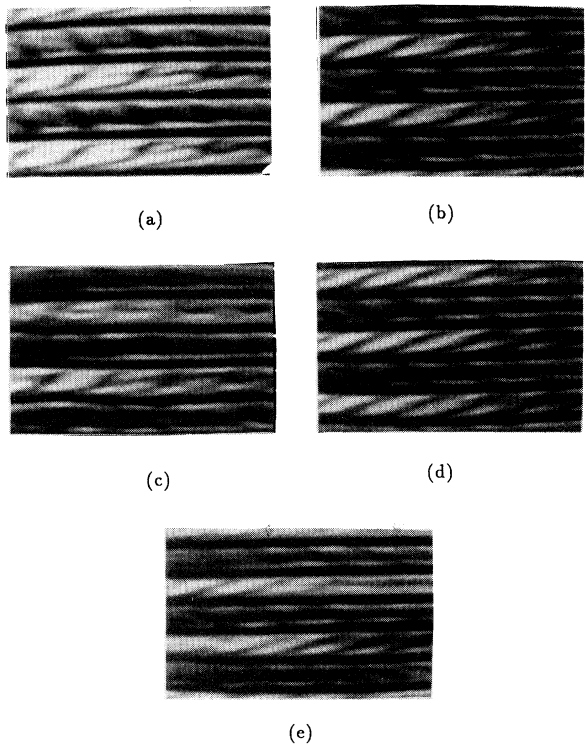

FIG. 3. Shown are the following photographs of twisted vortex flows (TWI): (a) at $R_o=550$, $R_i=900$, and $\bar{\lambda}=2.50$; (b) at $R_0=650$, $R_i=1000$, and $\bar{\lambda}=2.31$; (c) TWI plus wavy inflow boundaries (WIB) at $R_o=650$, $R_i=1200$, and $\bar{\lambda}=2.31$; (d) at $R_o=750$, $R_i=1050$, and $\bar{\lambda}=2.14$; (e) at $R_o=650$, $R_i=1000$, and $\bar{\lambda}=2.00$.

wavelength preference for WIB and TWI, and a short wavelength preference for WOB. At the smallest wavelength surveyed we have observed a WVF with only one azimuthal wave ($m=1$). In addition we have observed weak time dependent activity in the vortices prior to the onset of WVF, WIB, WOB, and TWI at each wavelength surveyed.

In the remainder of the paper we will present the detailed results of our experimental study of these bifurcations. We will first describe our system, data acquisition techniques, and procedures. This will be followed by a discussion of the flow regimes observed and how they depend on the axial wavelength. We will end with a comparison of our results with present theory.

II. APPARATUS

Our Taylor-Couette apparatus consists of two cylinders, each of which is driven by Compumotor stepper motors (model M83-93). The inner cylinder is made of black Delrin plastic and has a radius of $r_i=5.26$ cm, while the outer cylinder is made of Plexiglas and has a radius $r_o=5.96$ cm, giving a radius ratio $\eta=0.882$ and gap $d=r_o-r_i=0.70$ cm. The inner and outer cylinder radii are known to within ± 0.005 cm. Coaxial with the two cylinders is an independently rotating table also controlled by a Compumotor stepper motor (model M106-178). The rotating table makes it possible to make observations and measurements in the rotating frame of reference. Electrical connections to instruments are provided by 25 coaxial cables connected through brushes to the laboratory frame of reference. The Compumotor stepper motors are controlled through Compumotor indexers (models 172 and 2100). The rotation speeds are precise to 0.001 Hz and may be changed or ramped through computer control. In the procedures used here we ramp the speed of one of the motors while the other motor's speed is fixed. The inner cylinder is directly driven by one motor, while the outer cylinder is linked to the second motor by means two sprockets and a timing belt, which produces a speed reduction of the cylinder by a factor of 4.

By operating the apparatus in a controlled environment room, the fluid temperature is kept constant to within 0.1°C during a run. The resulting uncertainty in Reynolds number is 1% for moderate to large values of $R_{i,o}$.

In order to maintain consistent end conditions the working fluid region (the region of experimental interest) is bounded by two Teflon collars which are attached to

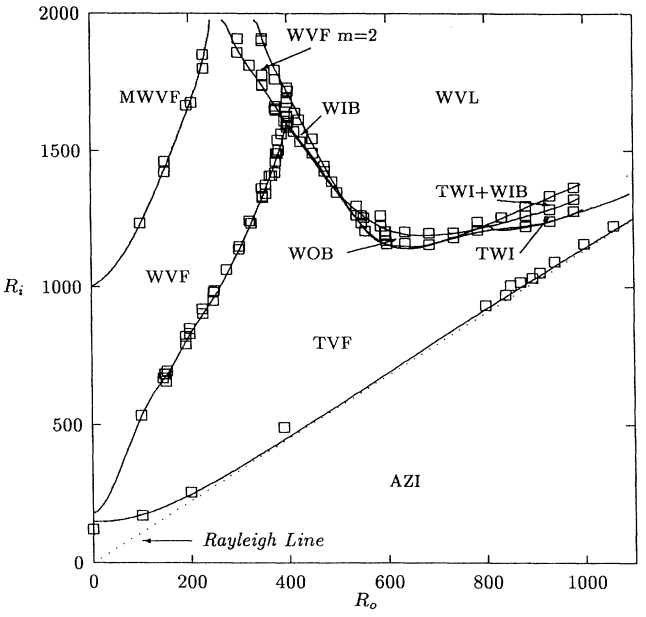

FIG. 5. The flow regime diagram for $N=30$ and $\Gamma=30$ ($\bar{\lambda}=2.00$). Labels refer to regions of stable states. The lines indicate the stability boundaries separating these stable states. Shown are the critical R_o and R_i for transitions to WVF, TWI, WIB, WOB, TWI+WIB, and WVL. The straight line above the *AZI* region is the Rayleigh stability line.

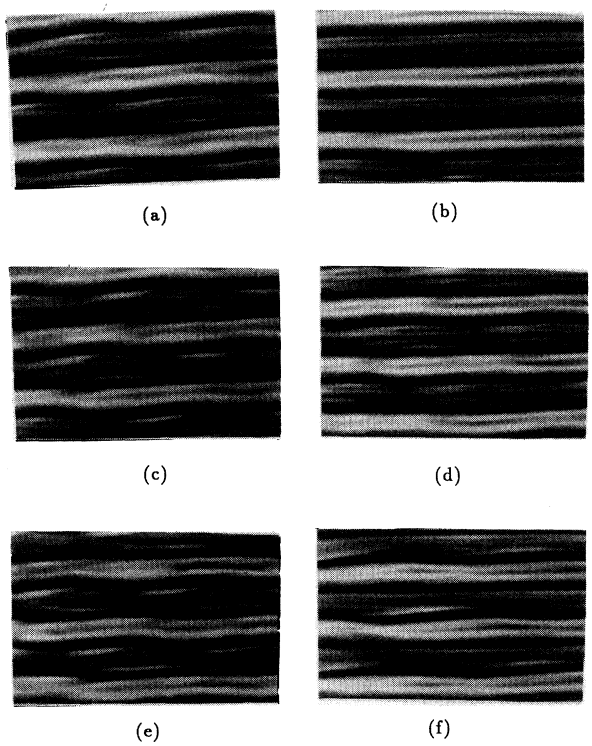

FIG. 4. Shown are the following photographs of wavy flows: (a) WIB at $R_o=650$, $R_i=1450$, and $\bar{\lambda}=2.31$; (b) WIB at $R_o=525$, $R_i=1450$, and $\bar{\lambda}=2.14$; (c) WVL at $R_o=600$, $R_i=1450$, and $\bar{\lambda}=2.14$; (d) WIB at $R_o=450$, $R_i=1450$, and $\bar{\lambda}=2.00$; (e) wavelets (WVL) at $R_o=500$, $R_i=1450$, and $\bar{\lambda}=2.00$; (f) wavy outflow boundaries (WOB) at $R_o=600$, $R_i=1100$, and $\bar{\lambda}=1.88$.

the outer cylinder by rubber O rings. The aspect ratio Γ ($\equiv l/d$, where l is the axial length of the working region) was fixed at 30 for this study, although the system will accommodate Γ up to 73 by changing the location of the Teflon rings. This aspect ratio is known within $\approx 1.0\%$. The Teflon collars ensure, via Ekman pumping, an inflow boundary at both the top and bottom boundaries and thus an even number of Taylor vortices in the working fluid region. We specify the local dimensionless axial wavelength, using d as our length scale, as $\lambda = \lambda^*/d$ where λ^* is the unscaled size of a particular vortex pair. This may or may not be identical to the average over all the vortices $\bar{\lambda} = 2\Gamma/N$, where N is the number of vortices in the system.

We used distilled water for our working fluid together with 1% by volume mixture of Kalliroscope AQ1000 for flow visualization. The Kalliroscope consists of an aqueous suspension of reflective $\approx 30 \times 6 \times 0.07$ μm^3 crystalline platelets [14]. We have maximized the contrast by viewing the flow radially toward the cylinders while illuminating the flow from nearly an axial direction. Savas [15] has made a quantitative analysis of reflective ellipsoidal particles suspended in a viscous fluid. His work shows that the particles tend to align along the stream surfaces (surfaces of constant velocity of the entire three dimensional (3D) flow, also called streamlines in a 2D flow) of the flow. Therefore the base Couette flow looks like a uniform cylinder because the stream surfaces are cylinders that are coaxial with the inner and outer cylinders. Any radial flow is indicated by a lack of reflection, revealing the black inner cylinder. The vortices in TVF look like donuts because their stream surfaces are approximately tori with their axes perpendicular to the cylinders' axes. The centers of the vortices appear white because the stream surfaces are primarily parallel to the cylinder wall in the (θ, z) plane (where r, θ, and z are the radial, azimuthal, and axial coordinates, respectively). The inflow and outflow boundaries appear dark because the stream surfaces are primarily in the (r, θ) plane. Because the stream surfaces in the center of the vortices tend to tilt radially outward near an outflow boundary and radially inward near an inflow boundary [6–9] there is a difference in the reflected brightness between adjacent Taylor vortices (see Fig. 1). Schwarz [16] has found that flakes which initially have random orientations will, when subjected to a shearing velocity field such as dV_r/dz, develop substantial alignment in the stream planes in a time of order $(dV_r/dz)^{-1}$. The flakes respond quickly to the change in the local velocity fields, especially in regions of strong shear. The distilled water is boiled prior to mixing with the Kalliroscope to remove dissolved air that sometimes leads to bubble formation on the end rings. The fluid mixture lasts 2–3 days before it deteriorates. The system is cleaned by flushing it with a dilute solution of NaOH, which dissolves the platelets. The NaOH is then flushed out with multiples rinses of distilled water. The presence of Kalliroscope may lead to gravity-induced Taylor vortex nonuniformities [17]. We have checked our results by slowly ramping the system with the rotation axis horizontal in order to ensure that gravity does not affect the results.

III. PROCEDURES AND DATA ACQUISTION

The initial step in any run is the establishment of the desired axial wavelength. The wavelength is varied by changing the number of vortex pairs for a fixed Γ. In general terms this is accomplished by slowly rotating the outer cylinder (keeping $R_o \leq 50$) and then quickly ramping R_i above the onset of TVF. This produces dislocations in the vortices that can rapidly be removed by increasing R_i to above 4000 where the vortices are highly turbulent. In this turbulent state the vortices rapidly become more uniform in size [18]. Depending on the exact protocol followed, different numbers of vortices will result. The procedure is repeated until the desired number of vortices is obtained. The system is then quickly ramped in parameter space into a WVF state where the vortices are allow to reach a more uniform axial wavelength. After some time the system is ramped to the initial point of the run and allowed to relax to a uniform TVF state. A uniform initial state is generally achieved within 30 min.

Baxter and Andereck [13] found, in the corotating case and once a uniform state had been produced, that the ramping rate had little effect on the secondary flow onset values if the dimensionless ramping [19] rate a, defined as

$$a = (dR_{i,o}/dt)[l(r_0 - r_i)/\nu] ,$$

was less than 20. We have kept to this protocol to ensure quasistatic conditions and consistency from run to run. For comparison, Park, Crawford, and Donnelly [19] found that, for the transition from Couette flow to TVF with a stationary outer cylinder, quasistatic conditions were achieved for $a \leq 10$.

The onset of instabilities in the visualized flow could sometimes be observed in real time. However, due to the low ramping rates necessary, time lapse video recordings were typically used to assist in the determination of these instability points. The video recorder (Panasonic model AG-6010) was usually set for a time interval between frames of 0.4 sec. This allowed the recording of 24 h of ramping on one 2 h video cassette. Since for the largest ramping rates used, velocity changes were made once a minute, and then in increments of only 0.000 25 Hz, the time resolution of the recorder was sufficient to obtain accurate onset values.

To monitor the wavelength of the Taylor vortices we used a linear 1024 pixel charge coupled device (CCD) camera. The line of pixels was oriented parallel to the cylinder axis and a telephoto lens formed an image of the visualized flow on the array. With our system size the resolution of the image was 0.2 mm. The signals from all 1024 pixels were digitized with a 12 bit analog to digital (A/D) converter and this frame was then sent to our computer. The computer averaged 50 randomly chosen frames, thus removing the effects of vortex boundary waves, and stored the result.

After either R_i or R_o has been ramped to the desired final value each set of averaged frames is analyzed. The positions of the inflow and outflow boundaries are found by least squares fitting of parabolas to the intensity minima. We know that adjacent to the two end collars are

the inflow boundaries of the Ekman-pumped cells. By locating the first minimum away from each collar the Ekman-pumped cell sizes are determined. The Ekman wavelength is the axial length of both Ekman-pumped cells. Next, the axial distance between every other minimum is found. This is the axial distance between consecutive inflow or outflow boundaries and thus also the local axial wavelength. The local wavelengths in the bulk are then averaged (the bulk excludes the vortex pairs immediately adjacent to the Ekman-pumped cells since they are sometimes influenced by end effects). The wavelengths in the bulk and the Ekman wavelengths are calculated for each averaged frame and displayed as a function of inner or outer cylinder Reynolds number.

We also used the CCD camera to record the light reflectance of the patterns along the axis of the system as a function of time to produce space-time diagrams. A frame (a 1024×1 array of intensity versus axial position data) was recorded every 0.14 s. The data are then processed and displayed in a two dimensional format with the intensity and time coordinates sharing an axis.

The radial and axial cross section of the flow was visualized by shining a high intensity planar sheet of white light radially into the gap. The light sheet was produced by either placing a slide of a thin slit into a slide projector or by passing high intensity white light through a thin slit cut into a screen placed next to the outer cylinder. This technique effectively visualizes the interior of the vortices and was used to determine the onset of the weak time dependent activity internal to the vortices.

We used a single point reflectance technique and a rotating table to determine the frequencies and azimuthal wave numbers of the WIB, WOB, and WVF [20] at selected parameter values. The azimuthal wave number is the integer number of wavelengths in one azimuthal traverse of the cylinders. Spectra of the flow were obtained by shining monochromatic laser light into the flow and collecting light reflected from the Kalliroscope with a photodiode. The signal from the photodiode was digitized and Fourier transformed to obtain a spectrum. This apparatus was mounted on a rotating table so that spectra of the time dependent flows could be taken in a rotating frame of reference that is coaxial with the corotating cylinders. As shown by Zhang and Swinney [20], the slope of a plot of azimuthal wave frequency versus table frequency is the negative of the azimuthal wave number while the x intercept is proportional to the wave speed.

To find the critical values of R_i and R_o for bifurcations from TVF to WVF, WOB, WIB, or TWI we tried both increasing R_i with fixed R_o and increasing R_o for fixed R_i. The transitions from TVF to WVF were only slightly affected by the different ramping procedures (shifting an amount comparable to the run-to-run repeatability). The transitions from TVF to WIB, WOB, or TWI were more sensitive to the ramping procedure. The Taylor vortices tended to remain more uniform at higher R_o if we fixed R_i and varied R_o instead. This is probably due to the larger end effects generated by Ekman pumping at higher R_o. Nonuniformities in the TVF wavelength cause some ambiguity in the onset values of instabilities since different size Taylor vortices have different onset values. We note, however, that for a run at a given N in the range of R_i and R_o surveyed, the variation in local wavelength $\Delta\lambda$ is smaller than the change in average wavelength $\Delta\bar{\lambda}$ between runs with different N ($\Delta\lambda\approx 0.1$ for $N=26$ while $\Delta\bar{\lambda}=0.19$ between $N=24$ and $N=26$, $\Delta\lambda\approx 0.05$ for $N=32$ while $\Delta\bar{\lambda}=0.12$ between $N=30$ and $N=32$). Although there is some uncertainty in the axial wavelength of the vortices at a given N, we argue that since $\Delta\lambda\leq\Delta\bar{\lambda}$ we are justified in plotting the flow regime diagrams for fixed Γ and N because the parameter spaces at different N do not overlap. A more precise procedure would involve continuously varying Γ during a run to maintain a constant λ, but this has not been attempted.

IV. RESULTS

The main results of this work are shown in Fig. 6–8, the flow regime diagrams for the $N=26$, 28, and 32 cases. Figures 5 and 9 are subsets of previous surveys [2,13]. Figure 10 is a composite of these results. These diagrams show the critical Reynolds numbers for bifurcations from Taylor vortices for a range of $\bar{\lambda}$ from 1.88 to 2.50. In all cases the bifurcations were found to be supercritical within experimental error, except as otherwise

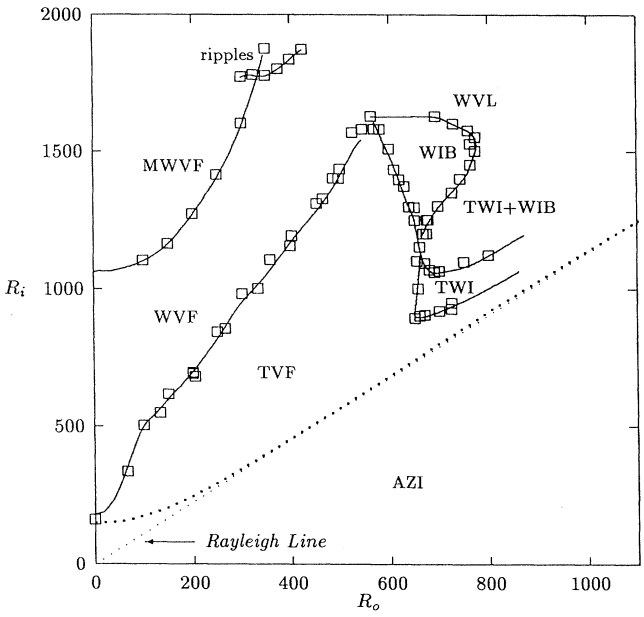

FIG. 6. The flow regime diagram for $N=26$ and $\Gamma=30$ ($\bar{\lambda}=2.31$). Labels refer to regions of stable states. The lines indicate the stability boundaries separating these stable states. Shown are the critical R_o and R_i for transitions to WVF, TWI, WIB, TWI + WIB, and WVL. The straight line above the *AZI* region is the Rayleigh stability line.

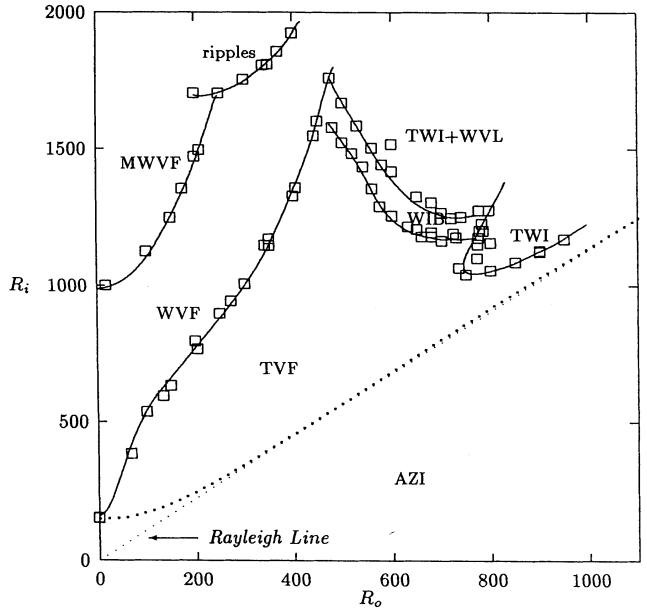

FIG. 7. The flow regime diagram for $N=28$ and $\Gamma=30$ ($\bar{\lambda}=2.14$). Labels refer to regions of stable states. The lines indicate the stability boundaries separating these stable states. Shown are the critical R_o and R_i for transitions to WVF, TWI, WIB, and WVL. The straight line above the *AZI* region is the Rayleigh stability line.

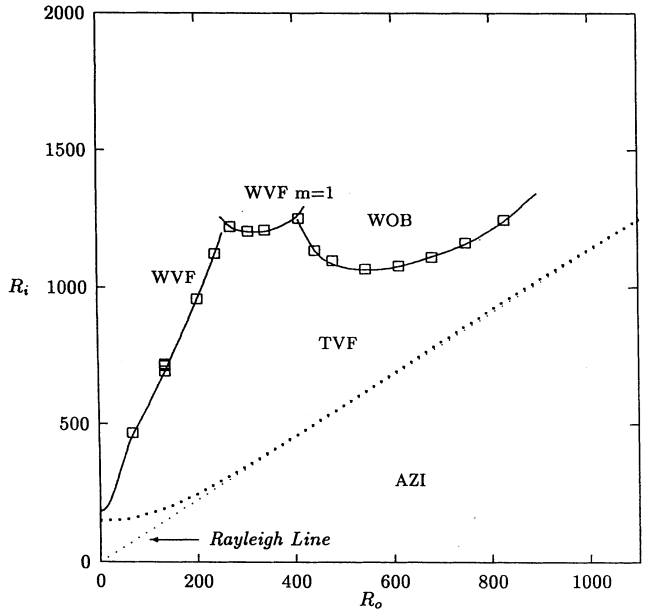

FIG. 8. The flow regime diagram for $N=32$ and $\Gamma=30$ ($\bar{\lambda}=1.88$). Labels refer to regions of stable states. The lines indicate the stability boundaries separating these stable states. Shown are the critical R_o and R_i for transitions to WVF, then $m=1$ WVF, and WOB. The straight line above the *AZI* region is the Rayleigh stability line.

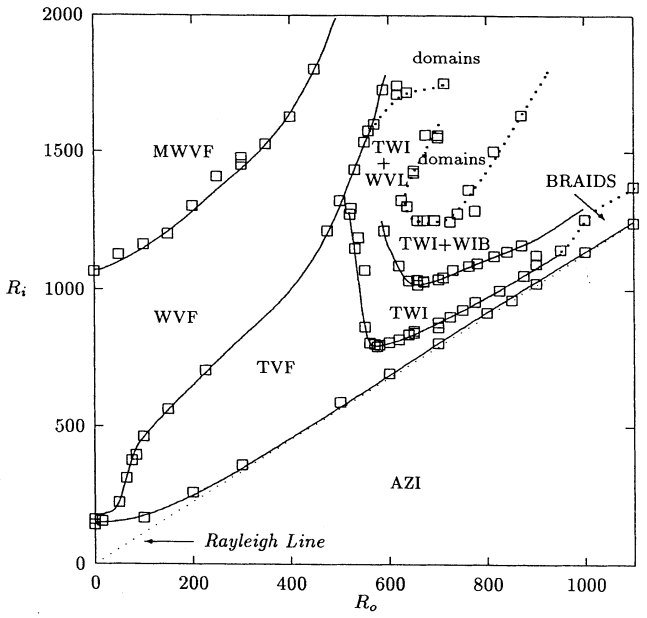

FIG. 9. The flow regime diagram for $N=24$ and $\Gamma=30$ ($\bar{\lambda}=2.5$). Labels refer to regions of stable states. The lines indicate the stability boundaries separating these stable states. Shown are the critical R_o and R_i for transitions to TVF, WVF, TWI, TWI+WIB, TWI+WVL, and domains. The straight line above the *AZI* region is the Rayleigh stability line. The Couette flow to TVF transition follows the Rayleigh line closely.

noted. It is apparent that the axial wavelength strongly affects which secondary flows will occur. WVF is present in the lowest range of R_o ($R_o \lesssim 450$) for all wavelengths surveyed. One tendency to note in Figs. 5–9 is that outer cylinder rotation delays the onset of WVF, with the result that the greater R_o is the greater the delay of WVF onset is with respect to R_i. Another tendency to note is

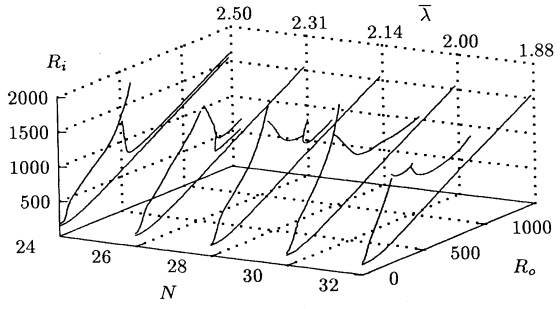

FIG. 10. The stability of Taylor vortex flow to other flows is shown in $(R_i, R_o, N=2\Gamma/\lambda)$ space. The stable region resembles a pork loin with slices at constant N having the shape of pork chops.

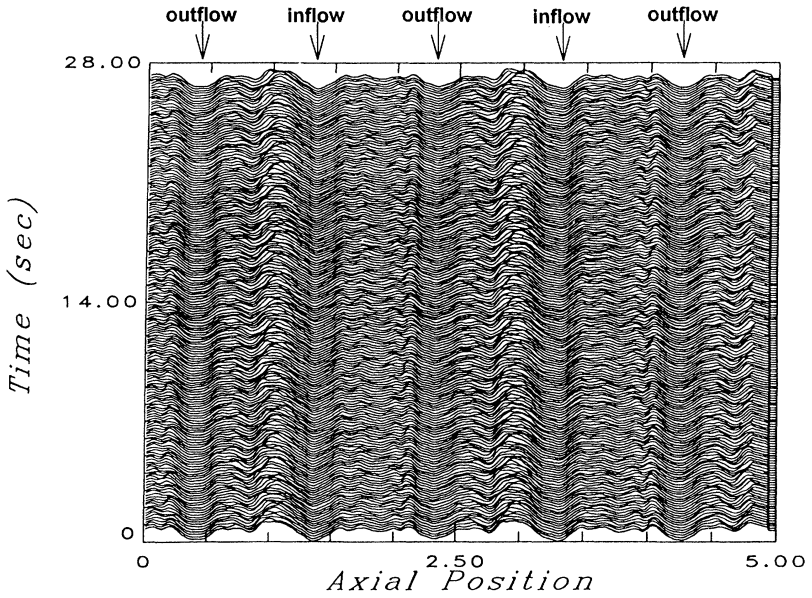

FIG. 11. Shown is the space-time diagram of the weak time dependent activity at $\bar{\lambda}=2.00$, $R_o=500$, and $R_i=1000$. Two inflow and three outflow boundaries are shown (the large intensity minima). Inside of these vortices are weaker dark lines that exhibit time dependence.

that the TVF to WVF transition line increases in slope as the average axial wavelength decreases (this effect was first noted by Coles [3]). In other words, compared to the larger wavelength vortices, smaller wavelength vortices at a given R_o suppress the onset of WVF to higher R_i. The most obvious differences for the various wavelengths occur in the fast outer cylinder rotation case ($R_o \geq 450$) where we observed TWI, WIB, WOB, and combinations of these. As can be seen in Fig. 8 transitions to WOB and WVF occur at $N=32$, including a transition to a novel $m=1$ WVF. WIB are not present for $N=32$. WIB, WOB, and TWI are all found for $N=30$, as can be seen in Fig. 5. The $N=26$ and 28 diagrams shown in Figs. 6 and 7 show that WIB are present at larger R_i and TWI are present at lower R_i. Waves form on the outflow boundaries only after WIB have formed and this combination is called wavelets (WVL) [2,10]. In Fig. 9 for $N=24$, the largest wavelength surveyed, TWI and TWI in combination with WIB [13] occur while WOB are absent. A comparison of the diagrams shows that increasing $\bar{\lambda}$ destabilizes TVF to TWI while stabilizing TVF against WIB and WOB. In summary, vortex pairs larger than the critical axial wavelength prefer WIB and TWI while vortex pairs smaller than the critical axial wavelength prefer WOB.

We also observed weak time dependent activity in TVF prior to the onset of WIB, WOB, and TWI. This weak activity was observed inside of the vortices using light sheet visualization. Prior to this activity dark lines inside of the vortices can be detected by illuminating the flow from an almost axial direction while observing the reflected light from a radial direction. These dark lines can be seen in the photographs of TVF shown in Fig. 1 and are present in WVF, WIB, and WOB at all the wavelengths surveyed, as can be seen in Figs. 1, 2, and 4. Corresponding to the weak time dependence seen with the light sheet visualization is the weak motion of these dark lines. The space-time plot in Fig. 11 shows this weak time dependence. The onset of the weak time dependent activity in TVF has been observed at $N=26$–32. The onset of this activity ranges from $\Delta R_o=100$ to 600 above

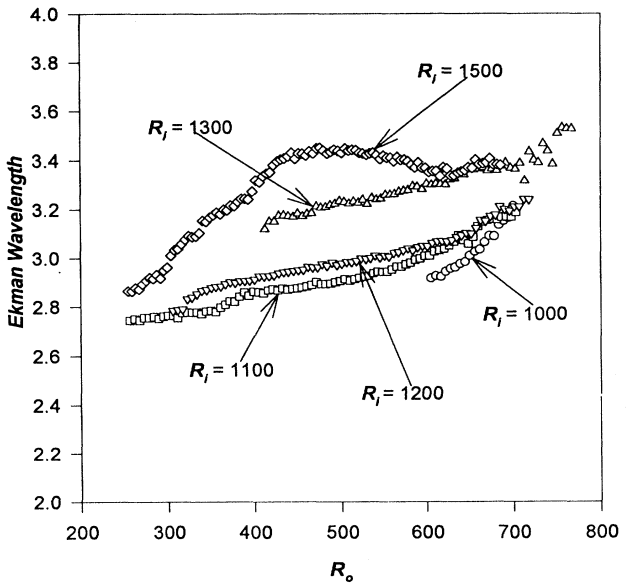

FIG. 12. The Ekman wavelength (the axial extent of the two end cells adjacent to the top and bottom collars) changes as R_o is ramped. The data were taken for $N=26$ and $\Gamma=30$ ($\bar{\lambda}=2.31$) at $R_i=1000$, 1100, 1200, 1300, and 1500.

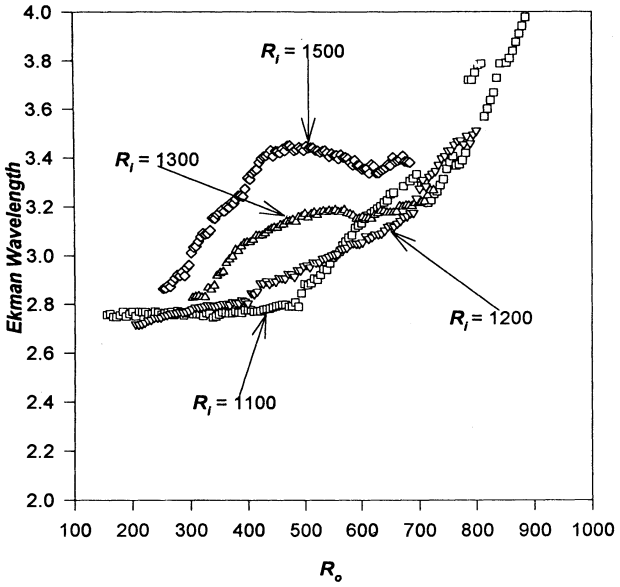

FIG. 13. The Ekman wavelength (the axial extent of the two end cells adjacent to the top and bottom collars) changes as R_o is ramped. The data were taken for $N=28$ and $\Gamma=30$ ($\bar{\lambda}=2.14$) at $R_i=1100$, 1200, 1300, and 1500.

the Rayleigh line for these wave numbers.

Our method for varying and maintaining the axial wavelength is limited by end effects. In particular the Ekman cells, and the vortex pairs adjacent to them, increase in size as R_o and R_i are increased. Since the aspect ratio is held constant the vortices in the bulk must decrease in wavelength. We found that for large R_o and $\bar{\lambda}$ the wavelength of the vortices in the bulk tended to stay more uniform if R_i was held constant as R_o was ramped. We show in Figs. 12 and 13 the variation of the sizes of the Ekman-pumped cells as R_o is ramped for $N=26$ and 28. In Fig. 14 we show some examples of the average axial wavelength of the vortices in the bulk at $N=26$ and 28. These figures show that the process of fixing the aspect ratio and varying the number of vortices may break down at some point because the average axial wavelength of the bulk may change too much. We reemphasize that the average axial wavelength of the vortices in the bulk at the transition points are well separated for large R_o for each flow regime diagram. This shows that our procedure for varying the wavelength was still meaningful for the parameter values necessary for observing bifurcations from TVF. The Ekman-pumped end cells also increase in size with R_o at $N=32$. As in the other cases the average wavelength in the bulk tends to decrease as the Ekman cell size increases. These axially compressed vortices tend to stay uniform when either R_o and R_i is ramped (in fact the data points in Fig. 8 were obtained by ramping R_o while R_i was held constant). They also tend to break down to an $N=30$ or 28 state, sufficiently far above onset, by developing dislocations that result in annihilation of vortex pairs. We have not attempted to survey the $N=34$ parameter region because of the difficulty in maintaining this state. We have also observed a novel combination of wavy flows near the Rayleigh line for large R_o ($R_o\approx900$) at $N=32$. As R_i is increased the thickness of each Taylor vortex becomes distorted azimuthally such that, in the laboratory frame, the axial wavelength of each vortex appears to alternately increase and then decrease. The largest distortions occur in the center of the working region with the vortices near

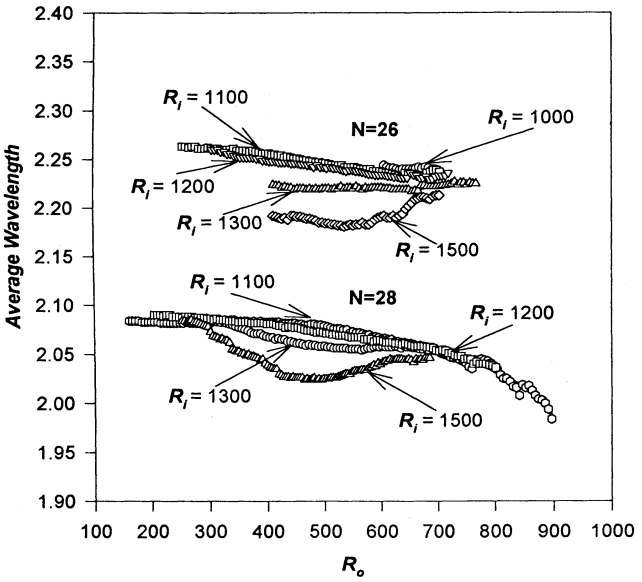

FIG. 14. The average wavelength (excluding the cells near the top and bottom collars) changes as R_o is ramped. The top data were taken for $N=26$ and $\Gamma=30$ ($\bar{\lambda}=2.31$) at $R_i=1000$, 1100, 1200, 1300, and 1500. The bottom data were taken for $N=28$ and $\Gamma=30$ ($\bar{\lambda}=2.14$) at $R_i=1100$, 1200, 1300, and 1500.

TABLE I. Wavy inflow boundary (WIB) experimental (m_e) and theoretical (m_t) azimuthal wave numbers at various N (numbers of vortices), R_o (outer cylinder Reynolds number), and R_i (inner cylinder Reynolds number).

m_e	m_t	N	R_o	R_i
12	12.8	30	450	1450
11	12.1	28	514	1450
10	11.1	26	607	1450

TABLE II. Wavy outflow boundary (WOB) experimental (m_e) and theoretical (m_t) azimuthal wave numbers at various N (number of vortices), R_o (outer cylinder Reynolds number), and R_i (inner cylinder Reynolds number).

m_e	m_t	N	R_o	R_i
10	14.5	34	600	1032
10	13.7	32	600	1080
10	12.8	30	600	1133

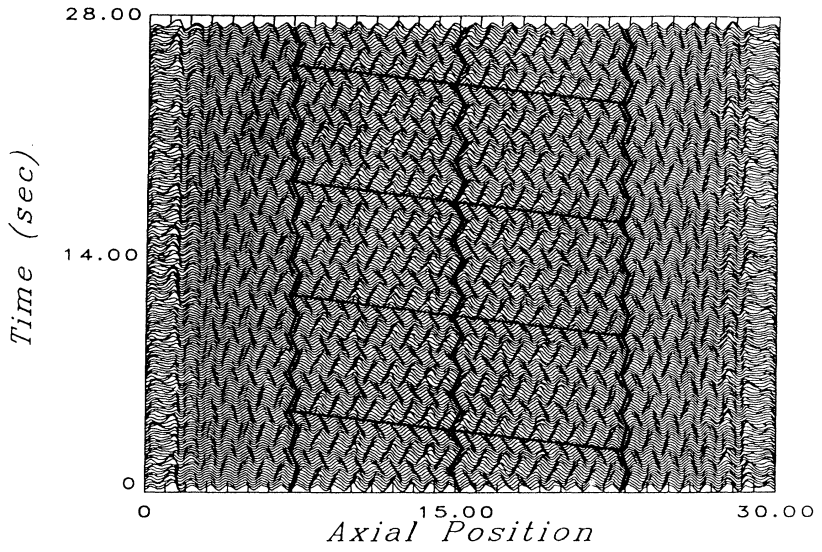

FIG. 15. Shown is the space-time diagram of the vortex thickness variations with TWI at the largest axial part of each vortex. The three oscillating dark lines which have been drawn on the figure each follow an intensity minimum of a vortex boundary as it moves up and down along the axis. The sloping lines between vortex boundary oscillations connect points of equal phase. This shows that they propagate along the cylinder axis with constant speed. This propagation is caused by the rotation of the spiral formed by the thick and thin parts of the vortices. This spiral pattern appears to propagate down the cylinder axis. These data were taken for $N=32$ and $\Gamma=30$ ($\bar{\lambda}=1.88$) at $R_o=950$ and $R_i=1275$.

the end cell almost unaffected. These distortions form a large scale pattern that appears to travel axially and azimuthally with the thick and thin parts of each vortex collectively forming a spiral. This spiral pattern becomes more apparent when, as R_i is increased, this large scale pattern distortion increases in amplitude and TWI form on the thick parts of the vortices. This large scale mode with a spiral of TWI is shown in the space-time diagram in Fig. 15 (the framing rate of our CCD camera is not high enough to resolve the TWI, WIB, or WOB in the laboratory frame). As R_i is increased WVL form on the thin parts of the vortices and a spiral of WVL and TWI forms. This state, shown in Fig. 16, is transient and can last for several hours before dislocations form which destroy one or two vortex pairs, leaving the system in an $N=30$ or 28 state.

As mentioned above, azimuthal wave numbers and wave speeds were measured at selected parameter values by taking several spectra in a rotating frame of reference at different table rotation speeds. Using this method we found that the central branch of the $N=32$ diagram is an $m=1$ WVF. We have also measured the azimuthal wave number and wave speed of the WIB and WOB at different $\bar{\lambda}$ but similar R_o and R_i (the R_o and R_i values were chosen such that the parameters would be as close as possible between wavelengths in order to compare az-

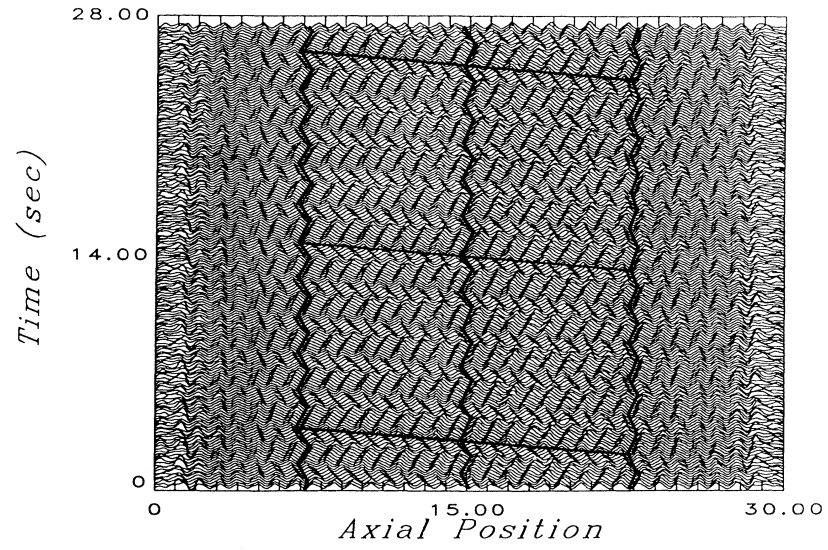

FIG. 16. Shown is the space-time diagram of the vortex thickness variations with TWI at the largest axial part of each vortex and WVL at the thinnest part of each vortex. As in Fig. 14 the thick and thin parts of the vortices form a rotating spiral. These data were taken for $N=32$ and $\Gamma=30$ ($\bar{\lambda}=1.88$), at $R_o=950$ and $R_i=1350$.

imuthal wave numbers and wave speeds at different axial wavelengths). Tables I and II show the results of these measurements. The WOB do not change in m as $\bar{\lambda}$ changes. The m of WIB increases by 1 each time N is increased by 2.

V. DISCUSSION OF RESULTS

In this section we examine the implications of the results presented above. We will give some qualitative arguments for the causes of these patterns given the weight of our results and previous experimental, numerical, and analytical results.

A. WVF

Several mechanisms have been suggested to explain the origin of the WVF instability at $R_o=0$. These mechanisms suggest that the local structure of the high speed flow regions between Taylor vortices becomes unstable. Because a fluid particle follows a roughly helical trajectory in a Taylor vortex, these high speed regions, or jets, have both azimuthal and radial velocity components. The following two scenarios focus on the azimuthal velocity components and the radial velocity components, respectively, of these jets. One scenario notes that the Taylor vortices produce an axially periodic azimuthal velocity with jets in the azimuthal flow in the inflow and outflow boundaries. In light of this fact it was suggested [7,21,22] that the WVF is caused by an Orr-Sommerfeld type of shear instability associated with inflection points in the axial variation of the azimuthal velocity (i.e., points where $\partial^2 V_\phi/\partial z^2=0$) which occur between the inflow and outflow boundaries. Jones [7] examined the stability of TVF for wide gaps ($\eta<0.8$) in order to understand a subharmonic wavy mode observed at $\eta\approx 0.5$ and $R_o=0$. This wavy mode, like WIB and WOB, repeats itself every 2λ with waves on adjacent outflow boundaries shifted by half a wavelength. Jones found that for wide gaps the azimuthal outflow jet is strong while the azimuthal inflow jet is weak. This suggests that a shear instability was responsible for the destabilization of the TVF because the waves only appear at the outflow boundary, where $\partial V_\phi(z)/\partial z$ is large. He also suggests that in small gap TVF, where both azimuthal jets are strong, this same mechanism destabilizes both the inflow and the outflow boundaries, causing WVF. Another scenario, given by Marcus [8], argues that a centrifugal instability due to the strong radial outflow jets leads to WVF, i.e., there is a local centrifugal instability in the Taylor vortices. In his scenario the radial outflow jet causes TVF to destabilize by locally violating the Rayleigh stability criterion, i.e., the angular momentum of the flow in the Taylor vortices decreases outward from their centers. Calculations by Marcus [8] of the WVF velocity field have shown that, for $\eta=0.875$ and $R_o=0$, the strong radial outflow boundaries that develop in TVF are diminished after the WVF instability develops. That is, the system finds a stable state by reducing this radial outflow kinetic energy while the energy in the azimuthal and axial velocity components increases. This increase is manifested as radial vorticity centered about the outflow boundary [8], just as would be expected from a centrifugal instability (centrifugal instabilities generally produce secondary flows with vorticity perpendicular to the vorticity of the primary flow, e.g., TVF or Dean rolls). In contrast, the shear instability scenario should lead to radial vorticity centered about the inflection points at the center of the vortices.

The TVF to WVF transition lines in all five flow regime diagrams have slopes greater than the slope of the Rayleigh line. This implies that the corotation of the outer cylinder suppresses the mechanism which destabilizes TVF to WVF. If WVF were the result of a shear instability associated with the inflection points in $V_\phi(z)$ one would not expect that corotating the outer cylinder would stabilize TVF against WVF. This is because the azimuthal jets result from the circulation in TVF and therefore the inflection points should appear after TVF has gained sufficient strength. At $R_o=0$ when the TVF to WVF transition occurs, the Taylor vortices are still relatively weak, i.e., they do not appear to have well-defined (high contrast) inflow and outflow boundaries. When $R_o>0$ the Taylor vortices appear to have well-defined inflow and outflow boundaries long before WVF appears. In fact the inflow and outflow boundaries are very sharp at approximately the same δR_i above the Rayleigh line. This suggests that the TVF to WVF instability line should be consistently close to the Rayleigh line, contrary to the data in Figs. 5–9. The centrifugal instability scenario, by contrast, gives a simpler qualitative understanding of the WVF transitions shown in Figs. 5–9. The TVF structure, in addition to modifying the azimuthal flow, produces a ϕ component of angular momentum per unit mass, L_ϕ. Coughlin and Marcus [9] have shown that the TVF structure neutralizes the basic centrifugal instability from Couette flow and that the WVF transition from TVF is associated with the strong outflow boundaries. They have also shown that at $R_o=0$ these outflow boundaries decrease in axial width as R_i increases. To see how a circulating vortex violates the Rayleigh stability criterion we need only examine L_ϕ, i.e., the flow in the cross section between the cylinders, ignoring the azimuthal flow. This is accomplished by defining a 2D polar coordinate system, (ρ,θ), at the center of a vortex. With this coordinate system the Rayleigh stability criterion is

$$\frac{\partial|\mathbf{L}_\phi|}{\partial\rho}\geq 0$$

and TVF will become centrifugally unstable (in the absence of viscosity) when

$$V_\theta+\rho\frac{\partial V_\theta}{\partial\rho}\leq 0\ .$$

The first term is always positive (V_θ is defined to be positive) while the second may be negative. In words, the vortex will tend to destabilize if V_θ decreases with distance away from the vortex core. Because the boundary condition forces this derivative to be negative near the cylinder walls, a significant viscous boundary layer must

exist there to stabilize TVF. Away from the wall, however, there is a destabilizing tendency which is observed in numerical simulations [6–9] and shown in Fig. 17. As R_i is increased the streamlines become concentrated toward the outer cylinder near an outflow boundary and toward the inner cylinder near an inflow boundary. This change in streamline shape pulls the maximum velocity streamline closer to the vortex core. This makes $\partial V_\theta/\partial \rho$ negative in the region where the streamlines are not concentrated. This potentially unstable region is toward the inner cylinder at an outflow boundary and toward the outer cylinder at an inflow boundary, as shown in the figure.

Increasing R_o at a given R_i is equivalent to decreasing the primary forcing of TVF. In fact, as can be seen in Figs. 5–9, one may start in TVF and increase R_o until Couette flow returns. This can also be understood by noting that the onset of TVF occurs above the Rayleigh line so that when the outer cylinder rotates TVF occurs at much larger average angular frequency of the cylinders $\overline{\Omega}=(\Omega_o+\Omega_i)/2$. In a frame of reference rotating with $\overline{\Omega}$ a fluid particle traveling radially outward is affected by a Coriolis force pulling it in the azimuthal direction. This weakens and spatially diffuses the radial outflow jet so that the inflow and outflow jets become more symmetric. The streamlines are forced into the more stable shapes with the maximum velocity streamline pushed back to the boundary layer. This changing of the streamline shapes gives us an explanation of why R_o stabilizes TVF against WVF.

The centrifugal instability and the Rayleigh criterion have their origins in the balance between the inertial forces of the circulating fluid and the pressure gradient in the fluid. Increasing the wavelength of TVF structures, i.e., elongating the structure in the axial direction, should increase the spatial extent of the potentially unstable regions. It should also, all other things being equal, decrease the bulk pressure gradient in the axial direction, $\delta P/\delta z$, between the vortex core and its boundaries. Because WVF affects the entire vortex this bulk decrease should also tend to destabilize the vortices, consistent with our observations that larger TVF wavelengths lead to WVF at lower R_i values.

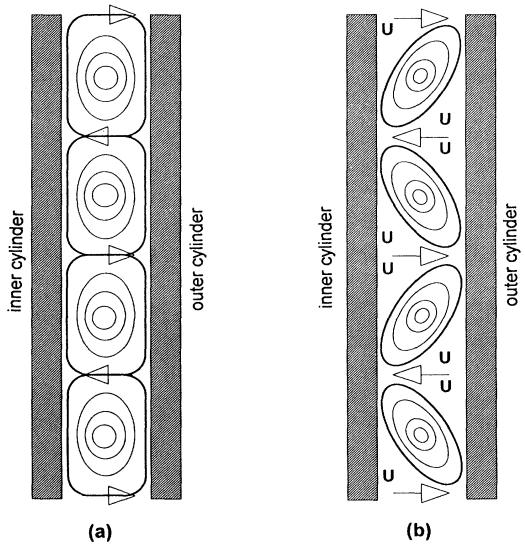

FIG. 17. Shown schematically are the projections of the streamlines in the axial plane (streamlines of the V_r and V_z velocity components) based on Refs. [6–9]. (a) The streamlines near onset. (b) The projections of the streamlines above onset where the streamlines become concentrated toward the outer cylinder near an outflow boundary and the streamlines become concentrated toward the inner cylinder near an inflow boundary. The maximum velocity streamline is indicated by a bold line. The areas marked with the **U** in (b) are the potentially centrifugally unstable regions due to the decrease in velocity away from the vortex center and the relatively large distance from the cylinder walls.

B. WIB and WOB

Although it appears that the centrifugal instability is the most likely scenario for WVF, at higher R_o there are other types of azimuthal traveling waves that form near Taylor vortex boundaries. These waves, the WIB and the WOB, occur at lower R_i values than one would expect for WVF. The WIB and WOB have a shorter azimuthal wavelength and a higher frequency than the WVF. These waves appear more localized than WVF, i.e., for WOB the inflow boundary is stationary and for WIB the outflow boundary is stationary. The stationary boundaries are not forced into motion by their oscillating neighbors, i.e., the oscillating neighbors are 180° out of phase. This subharmonic configuration of the WIB and WOB allows for an axial displacement of the oscillating inflow or outflow boundary without displacing their stationary neighbor boundary.

Because these waves form well below the R_i that one would expect for WVF (by extrapolating the WVF instability line) and the R_o is relatively large we do not expect the radial outflow jets to dominate as much as for WVF. In fact we expect the inflow and outflow boundaries to be of comparable magnitude. At $N=30$ the WIB and WOB transitions are quite close and cross twice as R_i and R_o are varied (see Fig. 5), indicating that these changes in R_i and R_o will slightly favor destabilization of one boundary over the other. The most striking feature of WIB and WOB is the systematic destabilization of TVF to WOB by axially compressed vortices and the destabilization of TVF to WIB by axially elongated vortices over a wide range of R_i and R_o, as shown in Figs. 6–9. Because both WIB and WOB are localized near a vortex boundary with almost no motion near the vortex center, it is likely that the radial vorticity generated by these waves is centered about the inflow or outflow boundary, indicating that these jets became centrifugally unstable. The centrifugal instability scenario implies that the axially elongated (compressed) vortices should have their maximum velocity streamlines near the walls at the outflow (inflow) boun-

daries so that the outflow (inflow) boundaries are stabilized. It also implies that a potentially unstable region with maximum velocity streamlines closer to the core should occur at the inflow (outflow) boundaries so that the inflow (outflow) boundaries are potentially unstable.

The large values of V_ϕ for this large R_o region of parameter space could make WIB and WOB good candidates for the shear instability scenario as well. Nagata's [6] calculations showed inflection points in the r-averaged $V_\phi(z)$ of TVF for corotating cylinders, especially when $\Omega_i-\Omega_o$ is small. Jones [7] used a simple model to describe the azimuthal velocity profile for $\Omega_o=0$, which we adopt here. It consists of a periodic V_ϕ that varies with z as a triangle wave. The stability of this approximate form of the azimuthal velocity profile can be calculated using Rayleigh's equation [21]. Jones found that the maximum growth occurs at azimuthal wave number $k=0.8031/(\lambda/4)$ where λ is the axial wave number. If m is, as before, the number of azimuthal waves, then the wave number is $k\approx 2m/(r_i+r_o)=2(1-\eta)m/d(1+\eta)$. Taking $\lambda\approx\bar{\lambda}d$ we get $m\approx 0.427N$. Tables I and II show that the results agree well with this model for WIB even though this model assumes that both the azimuthal inflow jet and the azimuthal outflow jet become unstable. The WOB, however, do not change azimuthal wave number with N, suggesting that either they are not a shear instability, or that the model breaks down for axially compressed vortices. The insensitivity of the WOB m to N implies that the disturbance is localized near the outflow jet as would be expected in the centrifugal instability scenario. On the other hand, the sensitivity of the WIB m to N may be because disturbances in axially elongated vortices are less localized than they are in axially compressed vortices. The WIB, which prefer axially elongated vortices, are sensitive to changes in N possibly because there is a larger region inside of the vortices that becomes centrifugally unstable. The negative result of the shear instability hypothesis for the WOB makes it likely that they are a result of a centrifugal instability while the WIB could be either.

C. Weak activity in TVF

The weak activity inside of TVF is characterized by dark lines near the vortex cores which fluctuate axially in time. These dark lines are indicative of radial flow and possibly small tertiary vortices. In addition to WIB and WOB, Nagata's [6] calculations also found another instability in which small vortices alternately grow and decay inside of neighboring Taylor vortices. These dark lines did not grow and decay, however, and the parameter values of the weak motion did not correspond to the parameter values of this predicted instability. The space-time diagram in Fig. 11 and the photograph in Fig. 1 show these dark lines. Before the weak time dependent activity begins the dark lines are stationary and first appear close to the onset of TVF. This suggests that weakly nonlinear theory may be able to describe the stationary lines. Davey [23] calculated an amplitude equation which showed that very close to onset a second harmonic in λ is generated which is time independent after saturation. Higher above onset many more stationary harmonics are generated as predicted by Davey [23] and measured by Heinrichs *et al.* [24]. It may be possible that these many harmonics produce this effect through a nonlinear mixing process.

At higher R_o the stationary lines begin to move. The fact that the time dependent activity does not grow in strength like WIB, WOB, WVF, or TWI suggests that it is not an instability but rather the result of some perturbations in the system exciting these harmonics. In support of this idea we have found that similar, but not sustained, time dependent activity can be generated by slightly changing the inner or outer cylinder frequency.

D. TWI

Figures 5–7 and 9 show that the TWI pattern bifurcates from TVF when R_o is large and R_i is close to the Rayleigh stability line. The figures also show that in the same range of parameter values the larger Taylor vortices are destabilized to TWI at lower R_o and R_i. Andereck, Dickman, and Swinney [4] reported that when the TWI pattern forms the secondary flow is strongest near the vortex core while the inflow and outflow boundaries are apparently undisturbed. Nagata [6] found a set of modes that become unstable at parameter values corresponding roughly to the parameter values of the TWI pattern observed by Andereck and co-workers [2,4]. The velocity field calculated by Nagata also reveals that the periodic motion is in the region of the vortex core. The centrifugal instability scenario could apply here because the wall forces $\partial V_\theta/\partial\rho$ negative between the inflow and outflow boundaries. The wall boundary layer, as noted above, also stabilizes the flow near the wall. If the maximum velocity streamline of TVF were closer to the core, however, this gradient could be negative farther away from the wall, leading to motion in the vortex core. In addition, Nagata reported an inflection point in the average azimuthal velocity implying the shear instability scenario. Here we present an alternative explanation.

The range of R_o and R_i where TWI form is characterized by a large average cylinder angular velocity $\bar{\Omega}=\Omega_0+\Omega_i/2$ and a small $\Delta\Omega=\Omega_o-\Omega_i$. To look at the behavior of the flow in the region of the vortex core we transform to the rest frame of a vortex core as follows (see Fig. 18). The origin of this coordinate system is placed at the center of a vortex, between the two cylinders, and rotates with the average speed of the cylinders. About this accelerating origin the system also rotates with $\bar{\Omega}$, the average angular velocity of the two cylinders, so that one of the axes, y', points in the inertial frame ϕ direction. This rotating frame also rotates about y' at Ω_t, the angular velocity of the flow about the vortex core, so that the core becomes approximately stationary. In other words $\bar{\Omega}$ points in the (inertial frame) axial direction and Ω_t points in the (inertial frame) azimuthal direction and this frame rotates at $\Omega=\bar{\Omega}+\Omega_t$ (this operation is similar to transforming from the inertial frame centered at the sun to the body centered frame of the rotating earth). The characteristic length in this

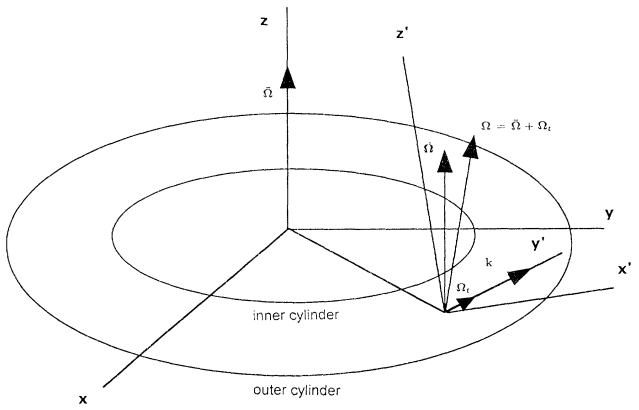

FIG. 18. The geometry for transforming from the inertial frame of reference (x,y,z) to the accelerating frame of reference (x',y',z'). The origin of the new axis rotates about the z axis. In addition the (x',y',z') axis rotates at $\bar{\Omega}=(\Omega_0+\Omega_i)/2$ and Ω_t, i.e., a total rotation of $\Omega=\bar{\Omega}+\Omega_t$. This frame follows the fluid in the vortex core so that this fluid is stationary in the (x',y',z') frame. The wave vector $\mathbf{k}$ of the inertial waves is directed in the azimuthal direction and the coordinate ζ points in the direction of Ω.

frame of reference is d and a characteristic velocity is $d\Delta\Omega$. With these scales the advective term $(\mathbf{V}\cdot\nabla)\mathbf{V}\sim d(\Delta\Omega)^2$ and the Coriolis force is $2\Omega\times\mathbf{V}\sim d\Delta\Omega\bar{\Omega}$. The advective term can be ignored in comparison to the Coriolis force if $\Delta\Omega/\bar{\Omega}\ll 1$. This is exactly the condition present when the TWI pattern appears. When this condition is satisfied the Navier-Stokes equations may be written as

$$\frac{\partial \mathbf{V}}{\partial t}+2\Omega\times\mathbf{V}=-\frac{1}{\rho}\nabla P ,$$

where the other fictitious forces are included in the pressure term [5]. We have assumed viscosity is negligible. If we take the curl of both sides to eliminate the pressure and take the direction of Ω to be the ζ axis then the equation can be written [5] as

$$\frac{\partial \nabla\times\mathbf{V}}{\partial t}=2\Omega\frac{\partial \mathbf{V}}{\partial \zeta} .$$

This equation has a plane wave solution [5] $\mathbf{V}=\mathbf{A}e^{i(\mathbf{k}\cdot\mathbf{r}-\omega t)}$. These waves, called inertial waves, are driven by the Coriolis force. They are also transverse $(\mathbf{k}\cdot\mathbf{A}=0)$ and circularly polarized [5]. Near the vortex core the fluid would appear to be approximately stationary, farther away from the core near the cylinders and near the radial jets the fluid would be in motion relative to this reference frame. In fact, away from the vortex core the Coriolis force would produce a forcing on the flow that would be approximately radially inward or outward near the cylinders and approximately azimuthally forward or backward near the radial jets. Thus there would appear to be a forcing in this rotating frame which could generate inertial waves. As the wavelength of TVF increases the flow becomes less circular closer to the core and this forcing would tend to increase, accounting for our results. The wave vector $\mathbf{k}$ points in the (inertial frame) azimuthal direction because the waves travel azimuthally along the vortex. This means that the velocity oscillates in the (inertial frame) axial (r,z) plane. Figure 3 shows typical TWI patterns where white and dark lines inside of each vortex are inclined relative to the inflow and outflow boundaries, indicating radial flow inside of each vortex. The inertial wave frequency is [5] $\omega=2\Omega\cos(\theta)$ in the rotating frame. Andereck *et al.* reported a 14 wave state with a frequency of $\approx 12.5\Omega_i$. If the TWI pattern were stationary in the rotating frame one would expect to see a frequency of $\approx 14\Omega_i$ in the inertial or laboratory frame, where we have used the approximation $|\Omega|\approx\Omega_i$. The difference could be accounted for by the inertial wave frequency which is less than $\simeq 2\Omega_i$.

An extensive numerical study of TWI has been performed by Weisshaar, Busse, and Nagata [25] in which they calculated the onset of TWI as a function of Reynolds number, rotation rate, and axial wavelength. They report that the bifurcation to TWI is supercritical, which agrees well with our finding of no detectable hysteresis in this transition. Some of their TWI onset data are plotted in Fig. 19 along with our experimental data. For the experimental data the λ shown is the wavelength of the vortices in the bulk which excludes the end vortices as discussed above. There is excellent agreement with the shapes of the onset lines, and there is reasonable agreement as to the positions of these onset lines.

The study of Weisshaar, Busse, and Nagata also finds TWI to be unstable to a skewed varicose type instability

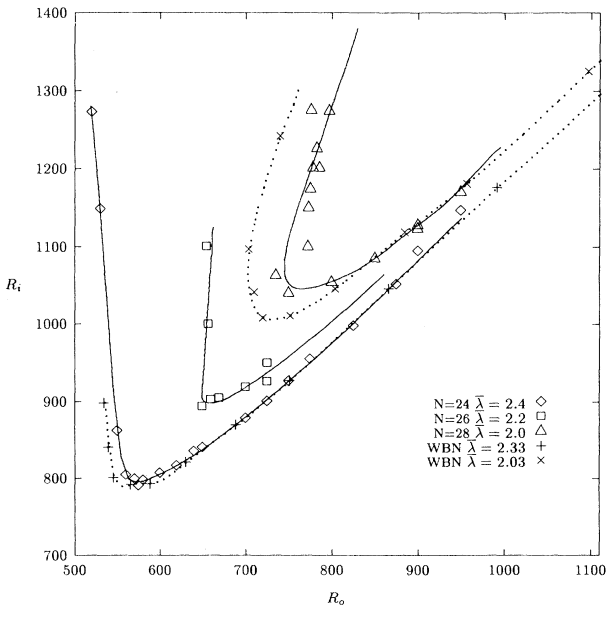

FIG. 19. The experimental data for the onset of TWI from TVF and the numerical results of Weisshaar, Busse, and Nagata (WBN) at comparable wavelengths.

at higher Reynolds numbers. Our results show that at $N=28$ there is a region of WVL+TWI above the TWI as shown in Fig. 7. Since WVL+TWI are vortices which have the TWI instability and have waves on both the inflow and outflow boundaries this flow is similar to the flow observed in the skewed varicose instability in Rayleigh-Bénard convection [25]. However, unlike the WBN results, we find this instability to be wavelength dependent. At $N=24$, 26, and 30 the TWI are bounded above by a region with waves on the inflow boundary only (TWI+WIB). This behavior is quite different from the skewed varicose instability.

Weisshaar, Busse, and Nagata have also found another twisted vortex solution they call "wavy twists." This solution has a much longer azimuthal wavelength, waves on both the inflow and outflow boundaries, and the same symmetry as WVF. Their numerical results predict the occurrence of this second solution over a wide range of axial wavelengths and at higher rotation rates than the TWI. For the parameter ranges studied here, we see no experimental evidence of "wavy twists."

E. Domains

Baxter and Andereck [13] observed domains of separate flow patterns characterized by distinctly different axial wavelengths. Nonuniform wavelength states have also been observed in Rayleigh-Bénard slot convection [26]. Brand and Deissler [27] have used a phase dynamics approach to describe such nonuniformities. In this work we observed similar phenomena at $N=26$ and 28. The system tended to develop a nonuniform axial wavelength after it was ramped above the threshold of secondary instabilities. Sometimes the TVF would develop weak nonuniformities at the onset of WIB or TWI and this would lead to either WIB or TWI in one part of the cylinder and TVF in the other. The only bimodality seen in the $N=32$ case was the TWI and WVL combination discussed above. These bimodal patterns varied both axially and azimuthally such that on each vortex there was an axial wavelength change (and an associated pattern change) as a function of azimuth.

In the numerical simulations of Weisshaar, Busse, and Nagata [25], TWI solutions are found to undergo an Eckhaus type instability over a wide range of $\bar{\Omega}$ and at all axial wavelengths. Although their simulation is unable to determine the final flow state following this instability, they cite the domains of large and small vortices at $N=24$ as a likely result. Although the domains at $N=24$ arise from twisted vortices with waves on one or both boundaries, the Eckhaus instability remains a likely explanation. We anticipate that the domains found at $N=26$ and 28 are probably due to the same instability. Busse and Auer [28] have also analyzed domain formation in Rayleigh-Bénard convection using an amplitude equation approach and cite these domains as an analogous case.

F. Stability of TVF

The stability of Taylor vortex flow is best shown with the volumetric plot of Fig. 10. The stable region resembles a pork loin with slices at constant N having the shape of pork chops. Because the end vortices are larger than the bulk vortices as discussed above, the axial wave number, $1/\lambda$, of bulk vortices is close to but larger than $1/\bar{\lambda}$. For convenience we have plotted $N=2\Gamma/\bar{\lambda}$. To a good approximation Fig. 10 is a representation of the volume of stable TVF in $(R_i,R_o,2\Gamma/\lambda)$ space. Clearly, TVF is most stable between $28<N<30$ which is where $\lambda=2.0$ would occur. At both larger and smaller values of N, TVF is found to be more unstable to other flows. At low R_o, TVF is always bounded above by WVF, and WVF occurs at lower R_i as N becomes smaller (or λ becomes larger). At higher R_o, TVF is bounded by a variety of flow states. Again, these bifurcations occur at increasingly lower values of both R_i and R_o as λ gets further from 2.0.

VI. CONCLUSION

By systematically surveying the $(R_o,R_i,\bar{\lambda})$ parameter space of Taylor vortices we have found the following basic results: increasing R_o stabilizes TVF against WVF; increasing $\bar{\lambda}$ destabilizes TVF against WVF and TWI while stabilizing TVF against WIB and WOB; WIB and TWI bifurcate from TVF for large $\bar{\lambda}$; and finally WOB bifurate from TVF for small $\bar{\lambda}$. We have also observed weak time dependent activity inside of the Taylor vortices before the onset of WVF, WIB, WOB, and TWI at all $\bar{\lambda}$ surveyed. At $\bar{\lambda}=1.88$, the smallest axial wavelength surveyed, we observed an $m=1$ WVF as well as a spiral of TWI and WVL. We measured the m values of WIB and WOB at different N (or $\bar{\lambda}$) and noted that the m of WIB depends on N while the m of WOB is independent of N. We have attempted to physically interpret our results with the help of previous numerical results. The most likely scenarios for these instabilities are a shear instability associated with the azimuthal jets near the inflow and outflow boundaries or a centrifugal instability associated with the radial inflow and outflow jets. Our judgment from the available evidence is that WVF and WOB are the result of a centrifugal instability. WIB, although very similar to WOB, may be either. The TWI pattern may be a result of inertial waves that form in the interior of the vortices. We have also visualized internal structure that may represent the axial harmonics predicted in weakly nonlinear theory and conjecture that the weak time dependent activity is not an instability but is related to weak driving by instrumental imperfections of these harmonics.

ACKNOWLEDGMENTS

This work was supported by ONR. Discussions with P. Marcus, H. Brand, H. Alfredsson, E. Weisshaar, and I. Mutabazi are gratefully acknowledged.

[1] R. C. Diprima and H. L. Swinney, in *Hydrodynamic Instabilities and the Transition to Turbulence,* edited by H. L. Swinney and J. P. Gollub (Springer-Verlag, New York, 1981), p. 139.
[2] C. D. Andereck, S. S. Liu, and H. L. Swinney, J. Fluid Mech. **164**, 1555 (1986).
[3] D. Coles, J. Fluid Mech. **21**, 385 (1965).
[4] C. D. Andereck, R. Dickman, and H. L. Swinney, Phys. Fluids **26**, 1395 (1983).
[5] L. D. Landau and E. M. Lifshitz, *Fluid Mechanics* (Pergamon, New York, 1987).
[6] M. Nagata, J. Fluid Mech. **169**, 229 (1986); **188**, 585 (1988).
[7] C. A. Jones, J. Fluid Mech. **157**, 135 (1985); also see **102**, 253 (1981).
[8] P. S. Marcus, J. Fluid Mech. **146**, 65 (1984).
[9] K. T. Coughlin and P. S. Marcus, J. Fluid Mech. **234**, 19 (1992).
[10] G. Iooss, J. J. Fluid Mech. **173**, 273 (1986).
[11] M. Golubitsky and I. Stuart, SIAM J. Math. Anal. **17**, 249 (1986).
[12] P. Chossat and G. Iooss, Jpn. J. Appl. Math. **2**, 37 (1985).
[13] G. W. Baxter and C. D. Andereck, Phys. Rev. Lett. **26**, 1395 (1986).
[14] P. Matisse and M. Gorman, Phys. Fluids **27**, 759 (1984).
[15] O. Savas, J. Fluid Mech. **152**, 235 (1985).
[16] K. W. Schwarz, Phys. Rev. Lett. **64**, 415 (1990).
[17] M. A. Dominguez-Lerma, G. Ahlers, and D. S. Cannell, Phys. Fluids **28**, 1204 (1984).
[18] M. Wu, C. D. Andereck, and H. R. Brand, Europhys. Lett. **19**, 587 (1992).
[19] K. Park, G. L. Crawford, and R. J. Donnelly, Phys. Rev. Lett. **47**, 1448 (1981).
[20] L. Zhang and H. L. Swinney, Phys. Rev. A **31**, 1006 (1985).
[21] P. G. Drazin and W. H. Reid, *Hydrodynamic Stability* (Cambridge University Press, Cambridge, England, 1981).
[22] K. A. Meyer, Los Alamos Report No. LA-3497, 1966 (unpublished).
[23] A. Davey, J. Fluid Mech. **14**, 336 (1962).
[24] R. M. Heinrichs, D. S. Cannell, G. Ahlers, and M. Jefferson, Phys. Fluids **31**, 250 (1988).
[25] E. Weisshaar, F. H. Busse, and M. Nagata, J. Fluid Mech. **226**, 549 (1991).
[26] J. Hegseth, J. M. Vince, M. Dubois, and P. Berge, Europhys. Lett. **17**, 413 (1992).
[27] H. R. Brand and R. J. Deissler, Phys. Rev. Lett. **63**, 508 (1989).
[28] F. H. Busse and M. Auer, Phys. Rev. Lett. **72**, 3178 (1994).

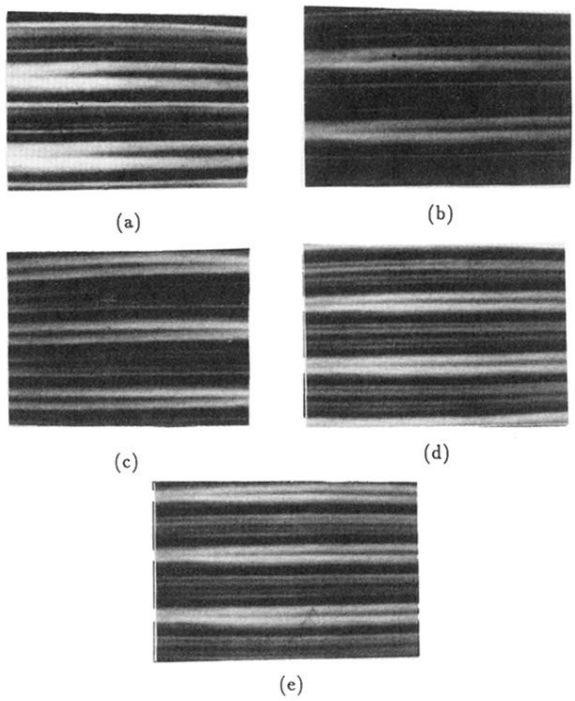

FIG. 1. Shown are the following photographs of Taylor vortex flows (TVF): (a) at $R_0=400$, $R_i=900$, and $\bar{\lambda}=250$; (b) at $R_0=500$, $R_i=1000$, and $\bar{\lambda}=2.31$; (c) at $R_o=500$, $R_i=1100$, and $\bar{\lambda}=2.14$; (d) at $R_o=400$, $R_i=1450$, and $\bar{\lambda}=2.00$; (e) at $R_o=350$, $R_i=1000$, and $\bar{\lambda}=1.88$. The azimuthal direction is along the parallel black lines (horizontal) and the axial direction is perpendicular to these lines (vertical). The black parallel lines are inflow and outflow boundaries. Between these black lines are vortices. Adjacent to each vortex is another vortex that circulates in the opposite sense. Neighboring vortices appear darker or lighter. Below each bright vortex is an outflow boundary and above each bright vortex is an inflow boundary. The distortion along the azimuth is due to the refraction effects in viewing the flow through the cylindrical outer cylinder.

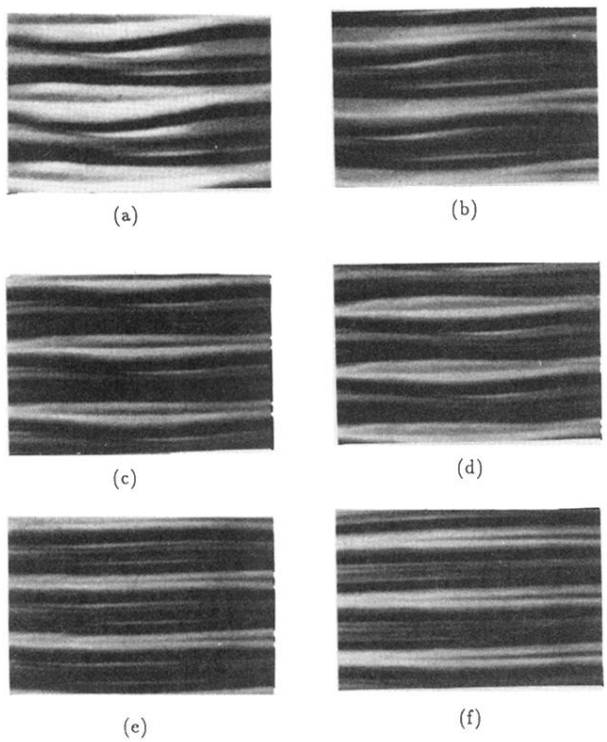

FIG. 2. Shown are the following photographs of wavy vortex flows (WVF): (a) at $R_o = 250$, $R_i = 900$, and $\bar{\lambda} = 2.50$; (b) at $R_0 = 300$, $R_i = 1000$, and $\bar{\lambda} = 2.31$; (c) at $R_o = 300$, $R_i = 1100$, and $\bar{\lambda} = 2.14$; (d) at $R_o = 300$, $R_i = 1450$, and $\bar{\lambda} = 2.00$; (e) at $R_o = 200$, $R_i = 900$, and $\bar{\lambda} = 1.88$; (f) $m = 1$ at $R_o = 350$, $R_i = 1100$, and $\bar{\lambda} = 1.88$.

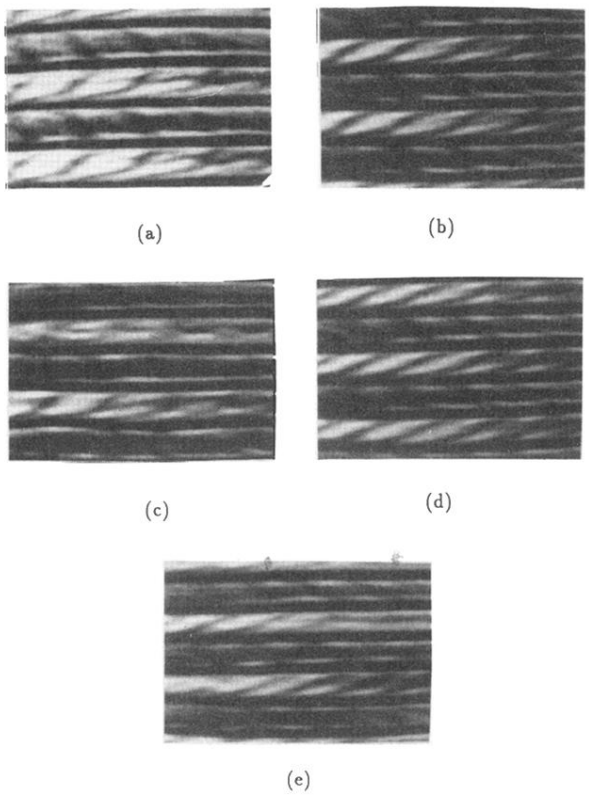

FIG. 3. Shown are the following photographs of twisted vortex flows (TWI): (a) at $R_o = 550$, $R_i = 900$, and $\bar{\lambda} = 2.50$; (b) at $R_0 = 650$, $R_i = 1000$, and $\bar{\lambda} = 2.31$; (c) TWI plus wavy inflow boundaries (WIB) at $R_o = 650$, $R_i = 1200$, and $\bar{\lambda} = 2.31$; (d) at $R_o = 750$, $R_i = 1050$, and $\bar{\lambda} = 2.14$; (e) at $R_o = 650$, $R_i = 1000$, and $\bar{\lambda} = 2.00$.

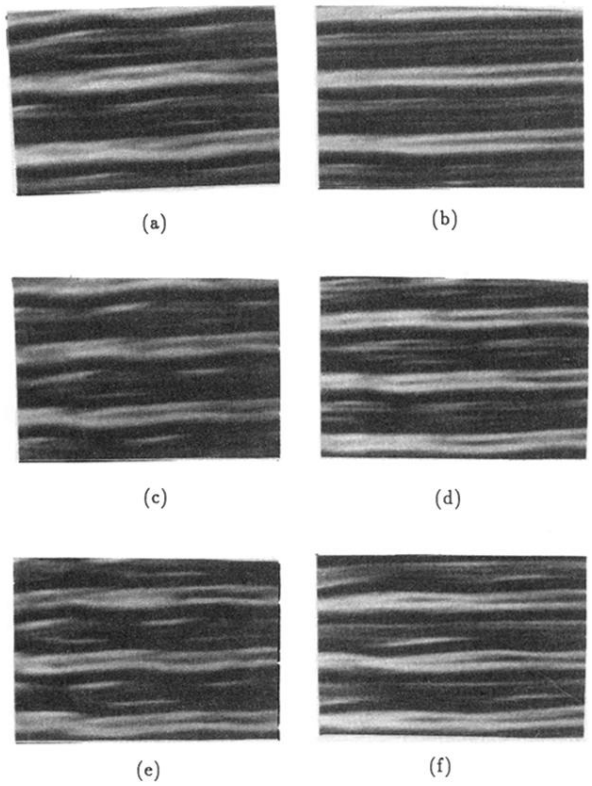

FIG. 4. Shown are the following photographs of wavy flows: (a) WIB at $R_o=650$, $R_i=1450$, and $\bar{\lambda}=2.31$; (b) WIB at $R_o=525$, $R_i=1450$, and $\bar{\lambda}=2.14$; (c) WVL at $R_o=600$, $R_i=1450$, and $\bar{\lambda}=2.14$; (d) WIB at $R_o=450$, $R_i=1450$, and $\bar{\lambda}=2.00$; (e) wavelets (WVL) at $R_o=500$, $R_i=1450$, and $\bar{\lambda}=2.00$; (f) wavy outflow boundaries (WOB) at $R_o=600$, $R_i=1100$, and $\bar{\lambda}=1.88$.